Corner modes in non-Hermitian next-nearest-neighbor hopping model

Arnob Kumar Ghosh ,[1,2,3] Arijit Saha ,[1,2,*] and Tanay Nag [4,†]
[1] *Institute of Physics, Sachivalaya Marg, Bhubaneswar 751005, India*
[2] *Homi Bhabha National Institute, Training School Complex, Anushakti Nagar, Mumbai 400094, India*
[3] *Department of Physics and Astronomy, Uppsala University, Box 516, 75120 Uppsala, Sweden*
[4] *Department of Physics, BITS Pilani-Hyderabad Campus, Telangana 500078, India*

(Received 8 March 2024; revised 20 July 2024; accepted 20 August 2024; published 3 September 2024)

We consider a non-Hermitian (NH) analog of a second-order topological insulator, protected by chiral symmetry, in the presence of next-nearest-neighbor hopping elements to theoretically investigate the interplay beyond the first-nearest-neighbor hopping amplitudes and topological order away from Hermiticity. In addition to the four zero-energy corner modes present in the first-nearest-neighbor hopping model, we uncover that the second-nearest-neighbor hopping introduces another topological phase with 16 zero-energy corner modes. Importantly, the NH effects are manifested in altering the Hermitian phase boundaries for both of the models. While comparing the complex energy spectrum under open boundary conditions, and bi-orthogonalized quadrupolar winding number in real space, we resolve the apparent anomaly in the bulk boundary correspondence of the NH system as compared to the Hermitian counterpart by incorporating the effect of the non-Bloch form of momentum into the mass term. The above invariant is also capable of capturing the phase boundaries between the two different topological phases where the degeneracy of the corner modes is evident, as exclusively observed for the second-nearest-neighbor model.

DOI: 10.1103/PhysRevB.110.115403

I. INTRODUCTION

The systems with topological band properties are identified with gapless boundary modes that are characterized by symmetry-protected topological invariants. This is known as bulk boundary correspondence (BBC) [1,2]. The conventional BBC, being an integral part of the first-order ($n = 1$) topological phase [1,3–5], is generalized for higher-order ($n > 1$) topological phases in $d \geqslant 2$ dimensions, where there exist $n_c = (d - n)$-dimensional boundary modes [6–40]. For example, the second-order topological insulator (SOTI) in two dimensions hosts zero-dimensional (0D) localized corner modes at zero energy, while this bulk phase is characterized by nested polarization or quadrupolar moment. Very recently, it has been reported that the number of boundary modes in a topological phase can be tuned by considering next-nearest-neighbor hopping terms [41–45], as well as by implementing periodic Floquet drive [39,46]. Once the extended model continues to preserve the chiral symmetry (CS), one can characterize the new topological phase by winding numbers in odd spatial dimension [47–49]. The number of degenerate zero-energy states at each boundary increases according to the enhancement of the range of the hopping amplitudes, as indicated by the winding number ensuring the BBC [50,51]. It is noteworthy that the one-dimensional winding number for the first-order topological systems becomes passive in the case of even-dimensional generalizations [52]. In contrast, the higher-order topological (HOT) phase in even spatial dimension can be characterized by an appropriately defined winding number, preserving CS as a constraint [53].

In recent years, thanks to the practical realization of higher-order topological phases in metamaterials [54–57] where energy conservation no longer holds [58,59], the domain of topological quantum matter can be extended to the non-Hermitian (NH) systems. With the coupling to the environment [60–62], disorder/interaction-mediated quasiparticles with finite lifetime [63–65] can effectively induce complex self-energy that is modeled by an NH effective Hamiltonian [59,66–72]. Interestingly, the non-Bloch nature of the wave function for the NH systems renormalizes the topological mass term, thus enriching the BBC such that topological phase transitions perceived with open-boundary conditions can be explained by an appropriate bulk invariant [73–80]. The NH topological systems showcase various intriguing features such as the skin effect where the bulk states accumulate at the boundary [73,74,76,81], and exceptional points where eigenstates, corresponding to the degenerate bands, coalesce [82,83].

Going beyond the scope of the first-nearest-neighbor (NN) hopping, the second-NN or the next-nearest-neighbor hopping elements in Hermitian systems are found to mediate versatile topological phases where the number of zero-energy modes increases [44,84–86]. In this context, the interplay between the next-NN hopping elements and non-Hermiticity is still in its infancy as far as HOT systems are concerned [75,87–91]. Therefore, considering a two-dimensional (2D) NH SOTI with next-NN hopping, we examine whether non-Hermiticity induces exceptional SOTI phases, otherwise absent in the

*Contact author: arijit@iopb.res.in
†Contact author: tanay.nag@hyderabad.bits-pilani.ac.in

Hermitian case, and address the following interesting questions: How does the BBC change in the above NH phases? Can we characterize these emerging exceptional topological phases by bi-orthogonalized non-Bloch winding number?

We consider a CS-preserved generic model, hosting SOTI phases in the presence of non-Hermiticity and next-NN hopping terms. The first- (second-) NN Hermitian model Hamiltonian can host four (four and 16) zero-energy corner modes, while exceptional points, caused by the NH effects, reshape topological phase boundaries as compared to the Hermitian case. As a result, we find that BBC is not only different from its Hermitian counterparts, but is also nontrivially modified once second-NN hopping terms are included. The phase boundaries between four (one) and one (zero) zero-energy modes per corner in the second- (first-) NN model are revised following the dressed mass term due to the non-Bloch nature of the wave function for the NH Hamiltonian. We compute the quadrupolar winding number (QWN) appropriately in real space by exploiting the CS as well as implementing the bi-orthogonalization and non-Bloch nature to lay out the phase diagram, which is in accordance with the complex spectrum under open-boundary conditions (OBCs).

The remainder of the article is organized in the following way. We discuss the details of the tight-binding Hamiltonian in Sec. II, where both the NH first and second hopping models are demonstrated. Section III is devoted to the main results of this article. In particular, we discuss the result associated with the first- and second-NN hopping models in Secs. III A and III B, respectively. Next, we illustrate the exceptional phase diagram in Sec. III C by examining the QWN. We finally summarize and conclude in Sec. IV. In Appendices A and B, we discuss the spatial symmetries of our model, the effect of asymmetric hoppings, and the finite-size effect with the NH second-NN hopping model.

II. MODEL HAMILTONIAN

We consider the SOTI model in the presence of the second-NN hopping as follows [87]:

$$H_0(\mathbf{k}) = \left(\lambda_1^s \sin k_x + \lambda_2^s \sin 2k_x\right)\Gamma_1 + \left(\lambda_1^s \sin k_y + \lambda_2^s \sin 2k_y\right)\Gamma_2 + \left[m_0 - \lambda_1^h(\cos k_x + \cos k_y) - \lambda_2^h(\cos 2k_x + \cos 2k_y)\right]\Gamma_3 + \left[\lambda_1^f(\cos k_x - \cos k_y) + \lambda_2^f(\cos 2k_x - \cos 2k_y)\right]\Gamma_4, \tag{1}$$

where $\Gamma_1 = \sigma_x s_z$, $\Gamma_2 = \sigma_y s_0$, $\Gamma_3 = \sigma_z s_0$, and $\Gamma_4 = \sigma_x s_x$. We consider the strengths of first- (second-) NN hopping, spin-orbit coupling, and C_4 symmetry-breaking mass terms as λ_1^h, λ_1^s, and λ_1^f, (λ_2^h, λ_2^s, and λ_2^f), respectively. Here, m_0 is the staggered mass term. In what follows, we refer to the case of $\lambda_1 \neq 0$ and $\lambda_2 = 0$ ($\lambda_{1,2} \neq 0$) as the first- (second-) NN model. In the absence of the second-NN terms, i.e., $\lambda_2^h, \lambda_2^s, \lambda_2^f = 0$ and $\lambda_1^h, \lambda_1^s, \lambda_1^f \neq 0$, the Hamiltonian $H_0(\mathbf{k})$ exhibits bulk gap closing at $m_0 = \pm 2\lambda_1^h$. One can show that the Hamiltonian $H_0(\mathbf{k})$ exhibits four zero-energy corner modes arising within the regime $-2\lambda_1^h < m_0 < 2\lambda_1^h$, manifesting a SOTI. Note that in the absence of Wilson-Dirac mass terms $\lambda_{1,2}^f = 0$, one obtains gapless edge modes for $-2\lambda_1^h < m_0 < 2\lambda_1^h$ except for $m_0 = 0$. This indicates the fact that the first-order topological insulator phase completely transforms into the second-order topological insulator phase. Furthermore, the presence of second-NN terms, i.e., $\lambda_2^h, \lambda_2^s, \lambda_2^f \neq 0$ and $\lambda_1^h, \lambda_1^s, \lambda_1^f \neq 0$, substantially modifies the phase boundaries. To be specific, the bulk gap closes at $m_0 = -2\lambda_2^h, 0, 2\lambda_1^h + 2\lambda_2^h$. In this case, the system harbors four zero-energy corner modes for $-2\lambda_2^h < m_0 < 0$, while 16 zero-energy corner modes for $0 < m_0 < 2\lambda_1^h + 2\lambda_2^h$. Similar to the earlier case, in the absence of Wilson-Dirac mass terms $\lambda_{1,2}^f = 0$, one obtains the gapless edge modes for $-2\lambda_2^h < m_0 < 2\lambda_1^h + 2\lambda_2^h$ except for $m_0 = 0$. Note that this model also hosts a first-order topological insulator phase for $-2\lambda_1^h < m_0 < 2\lambda_1^h$ and $-2\lambda_2^h < m_0 < 2\lambda_1^h + 2\lambda_2^h$, respectively, when $(\lambda_1^f, \lambda_2^f) = (\neq 0, 0)$ and $(\neq 0, \neq 0)$. The above model preserves CS $C = \sigma_x s_y$ such that $CH_0(\mathbf{k})C^{-1} = -H_0(\mathbf{k})$. Importantly, the time-reversal symmetry $T = i\sigma_0 s_y \mathcal{K}$ is broken when $\lambda_{1,2}^f \neq 0$ such that $TH_0(\mathbf{k})T^{-1} \neq H_0(-\mathbf{k})$, with $\mathcal{K}$ being the complex conjugation. Note that $T^2 = -1$ leads to the AII class with a $\mathbb{Z}_2$ classification of the first-order topological phase.

Having demonstrated the physics of the Hermitian SOTI model, we now focus on the NH version of the above. We associate the NH effect to the spin-orbit-coupling part of the above Hamiltonian: $H_\gamma(\mathbf{k}) = H_0(\mathbf{k}) + i(\gamma_x\Gamma_1 + \gamma_y\Gamma_2)$, resulting in $H_\gamma^\dagger(\mathbf{k}) \neq H_\gamma(\mathbf{k})$. We consider $\gamma_x = \gamma_y = \gamma$, unless mentioned otherwise. The non-Hermiticity considered here can be thought of as an imaginary fictitious Zeeman field [68,87]. The CS continues to be preserved as $CH_\gamma(\mathbf{k})C^{-1} = -H_\gamma(\mathbf{k})$. We exploit the CS to define the NH analog of the quadrupole moment in real space (see later text for discussion). Note that for a NH Hamiltonian, the CS is often also referred to as a sublattice symmetry [69]. In the rest of the paper, we consider $\lambda_{1,2}^h = 1$ for the sake of simplicity.

III. RESULTS

In this section, we discuss the main results of this manuscript. We analyze the eigenvalue spectra and local density of states (LDOS) corresponding to our NH model with first- and second-NN hopping. Afterward, we define the quadrupolar winding number for our system and demonstrate the phase diagram.

A. NH model with first-NN hopping

We begin with the energy dispersion of the NH SOTI model in the presence of the first NN, as shown in Figs. 1(a)–1(c) [Figs. 1(d)–1(f)], under the periodic boundary condition (PBC) [(OBC)]. While employing PBC, we find $\mathrm{Re}[E] = 0$ for $2 - \tilde{\gamma} < m_0 < 2 + \tilde{\gamma}$ and $-2 - \tilde{\gamma} < m_0 < -2 + \tilde{\gamma}$, with $\tilde{\gamma} = \sqrt{2\gamma^2}$ around $m_0 = \mp 2$, as depicted by the

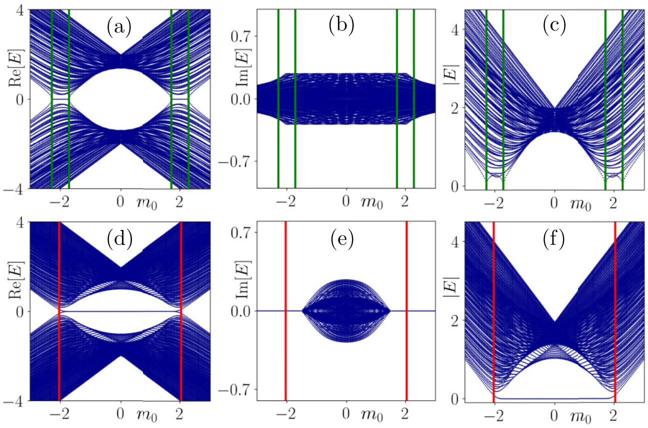

FIG. 1. The energy spectra under PBC and OBC are illustrated as a function of the staggered mass term m_0 in the upper and lower panels, respectively, for first-NN hopping. The above panels correspond to (a),(d) Re[E], (b),(e) Im[E], and (c),(f) $|E|$. The model parameters are chosen as $\lambda_1^s = \lambda_1^h = \lambda_1^f = 1.0$, and $\gamma = 0.2$. Here, green lines correspond to the exceptional points obtained from the PBC case $m_0 = \pm 2 \pm \tilde{\gamma}$. The red lines, representing the exceptional phase boundary under OBC, are given by $m_0 = \pm(2 + \gamma_1^2)$.

gapless regions in Fig. 1(a), bounded by the green lines. These exceptional boundaries around $m_0 = 2, -2$, respectively, can be understood from the twofold degeneracies of energy bands at $\mathbf{k} = (0, 0)$ and (π, π) such that $|E(\mathbf{k}_{\rm EP})| = 0$. Interestingly, these bulk gapless exceptional points $m_0 = \pm 2 \pm \tilde{\gamma}$ are exclusively noticed in $|E|$ under the PBC case, as depicted in Fig. 1(c) by the green lines.

We find that the complex energy spectra obtained under OBC and depicted in Figs. 1(d)–1(f) do not mimic the underlying PBC nature. One can observe SOTI modes for which the real part of the energy vanishes according to $-2 - \gamma_1^2 < m_0 < 2 + \gamma_1^2$, with $\gamma_1 = \gamma/\lambda_1^s$, as depicted by the red lines in Fig. 1(d). These boundaries can be anticipated by the non-Bloch form of momentum $k_i \to k_i' - i\gamma/\lambda_1^s$, with $i = x, y$, where the renormalized mass term $m_0' = m_0 - 2 - \gamma_1^2 < 0\,(> 0)$ determines the topological (trivial) phase of the NH model [68,87]. Note that for Bloch momentum $\mathbf{k} = (0, 0)$ [$\mathbf{k} = (\pi, \pi)$], the exceptional phase boundaries extend until $m_0 = \pm(2 + \gamma_1^2)$, leading to the emergence of exceptional SOTI phases beyond the Hermitian gapless phase boundaries $m_0 = \pm 2$. All the single-particle energy states under OBC except the corner modes exhibit an imaginary component of energy for $|m_0| < 2$, as shown in Fig. 1(e). This is markedly different from the PBC case, depicted in Fig. 1(b), where single-particle states have a finite amount of imaginary energy for $|m_0| > 2$. This refers to a macroscopic degeneracy within a certain range of m_0 as far as the Im[E] is considered. Since such macroscopic degeneracy does not exist for Re[E], the $|E|$ demonstrates the NH corner modes for $|m_0| < |2 + \gamma_1^2|$ under OBC [see red lines in Fig. 1(f)], while non-Hermiticity mediated bulk gapless points are noticed for the PBC case [see Fig. 1(c)].

Having understood the generation of the NH SOTI phase as a function of the topological mass m_0, we consider a slice with $m_0 = 1$ from Fig. 1 and analyze the results presented in Fig. 2.

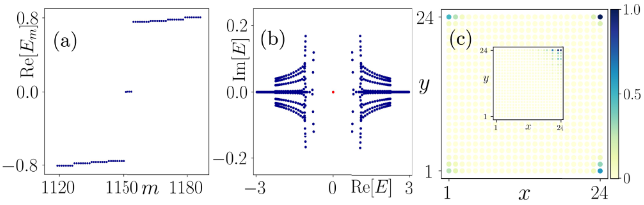

FIG. 2. (a) The real part of the energy eigenvalue spectrum, Re[E_m], obtained under OBC is shown as a function of the state index m. (b) The eigenvalue spectrum in the Re[E]-Im[E] plane is illustrated. The eigenvalues corresponding to the corner state are marked by the red dots. (c) The LDOS spectrum associated with the Re[E] = 0 is depicted in the 2D domain. Inset: The LDOS associated with a bulk state with $E = -2.052\,543$. We choose $m_0 = 1.0$, while the other model parameters remain the same as mentioned in Fig. 1.

In particular, employing OBC, we depict the real part of the eigenvalue spectrum Re[E_m] close to Re[E] = 0 as a function of the state index m in Fig. 2(a). We observe the appearance of four states at Re[E] = 0, which corresponds to localized corner states. In Fig. 2(b), we illustrate the eigenvalue spectrum in the Re[E]-Im[E] plane. The corner modes are marked by the red dot, which indicates that the corner modes have both real and imaginary parts of the eigenvalue equal to zero. The CS of the model is reflected in the symmetric profile of energy on the positive and negative sides of the real energy. The corner states (red) are clearly separated from the other states (blue) by a line gap at Re[E] = 0. Moreover, we show the site-resolved LDOS distribution in Fig. 2(c). We find that the corner modes are mostly localized at only one corner of the 2D domain. This phenomenon of the localization of the corner modes limited to only one corner of the system has been previously investigated in NH higher-order systems where mirror symmetries play a crucial role [75,87]. In particular, the localization of the states at a single corner of the 2D domain can be attributed to the mirror rotation symmetry M_{xy}. By changing the signs of the NH terms γ_x and γ_y, we can change the location of the corner states. By breaking the mirror rotation symmetry for $\gamma_x \neq \gamma_y$, we can localize the corner states at more than one corner. We discuss different spatial symmetries of the system and shifting of the corner modes in Appendix A. In the inset of Fig. 2(c), we also show the LDOS distribution associated with a bulk state. We observe that the bulk state is also localized at the corner of the system, indicating the existence of a higher-order skin effect [81].

B. NH model with second-NN hopping

To start with, we depict the energy dispersion of the NH SOTI model in the presence of the second NN in Figs. 3(a)–3(c) [Figs. 3(d)–3(f)] under PBC [OBC]. We find a degenerate eigenstate with Re[E] = 0 under PBC for $-2 - \tilde{\gamma} < m_0 < -2 + \tilde{\gamma}$, $-\tilde{\gamma} < m_0 < \tilde{\gamma}$, and $4 - \tilde{\gamma} < m_0 < 4 + \tilde{\gamma}$, as depicted by the green lines in Fig. 3(a). These exceptional boundaries around $m_0 = -2$, 0, and 4, respectively, can be understood from the twofold degeneracies of energy bands at $\mathbf{k} = (\pm 2\pi/3, \pm 2\pi/3)$, (π, π), and (0,0) such that $|E(\mathbf{k}_{\rm EP})| = 0$. Similar to the earlier first-NN model, these bulk gapless exceptional points $m_0 = -2 \pm \tilde{\gamma}$, $\pm\tilde{\gamma}$, and $4 \pm \tilde{\gamma}$ are exclusively

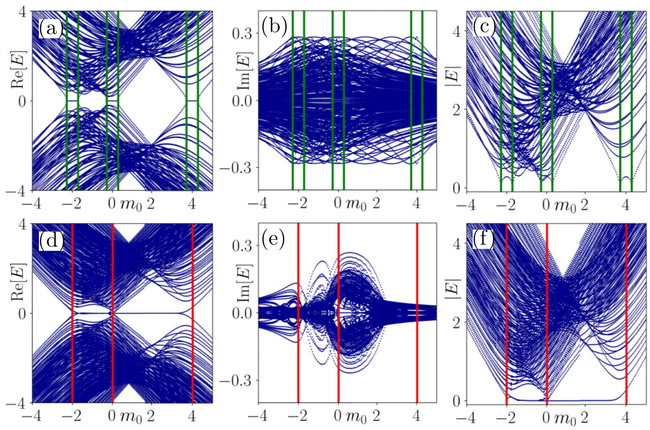

FIG. 3. The energy spectra under PBC and OBC are illustrated in the upper and lower panels, respectively, as a function of m_0, for second-NN hopping. The panels correspond to (a),(d) Re[E], (b),(e) Im[E], and (c),(f) $|E|$. We choose the model parameters as $\lambda_1^s = \lambda_1^h = \lambda_1^f = 1.0$, $\lambda_2^s = \lambda_2^h = \lambda_2^f = 1.0$, and $\gamma = 0.2$. The green lines correspond to the exceptional points $m_0 = 4 \pm \tilde{\gamma}$, $\pm\tilde{\gamma}$, and $-2 \pm \tilde{\gamma}$ under PBC. The red lines, representing the exceptional phase boundary under OBC, are given by $m_0 = 4 + 5\gamma_2^2$, $3\gamma_2^2$, and $-2 - \gamma_2^2$.

observed in $|E|$ for the PBC case, as depicted in Fig. 3(c) by green lines.

We now examine the energy spectrum for the second-NN model in Figs. 3(d)–3(f) employing OBC. Similar to the first-NN case, the momentum takes the following non-Bloch form: $k_i \to k_i' - i\gamma_2$ with $\gamma_2 = \gamma/(\lambda_1^s + 2\lambda_2^s)$, and $i = x, y$. This leads to the renormalized mass term $m_0' = m_0 - 4 - 5\gamma_2^2 < 0\,(> 0)$ for the topological (trivial) phase with zero-energy (finite-energy bulk) modes considering the Bloch momentum $\mathbf{k} = (0, 0)$. On the other hand, another topological (trivial) phase with zero-energy (finite-energy) modes appears for $-m_0' = m_0 + 2 + \gamma_2^2 > 0\,(< 0)$ while exploiting energy around the Bloch momentum $\mathbf{k} = (\pm 2\pi/3, \pm 2\pi/3)$. Our analysis indicates the existence of four (16) corner modes for $3\gamma_2^2 < m_0 < 4 + 5\gamma_2^2$ $(-2 - \gamma_2^2 < m_0 < 3\gamma_2^2)$, yielding Re[$E$] $= 0$ under OBC. However, the numerical findings shown in Fig. 3(d) and the topological regime highlighted by the red lines do not fully match with the exceptional boundaries predicted analytically. This can be attributed to the finite-size effect in the second-NN case, which is substantially small for the first-NN case. In particular, the rightmost boundary in Fig. 3(d) is more affected due to the finite-size scaling as there exists a significant mismatch between the analytical prediction $m_0 = 4 + 5\gamma_2^2$ and real zero-energy modes obtained under OBC. To this end, we discuss the finite-size scaling around the phase transition point at the rightmost part of Fig. 3(d) in Appendix B. Note that the finite-size effect is expected to become more substantial in the case of OBC, rather than for PBC. For this reason, we choose the phase boundary at $m_0 = 4 + 5\gamma_2^2$ for the finite-size analysis. We find macroscopic degeneracies at Re[E] $= 0$ around $m_0 = 0$, unlike the previous case. The complex energy spectrum Im[E] does not manifest any noteworthy features, as shown in Figs. 3(b) and 3(e), irrespective of the PBC and OBC

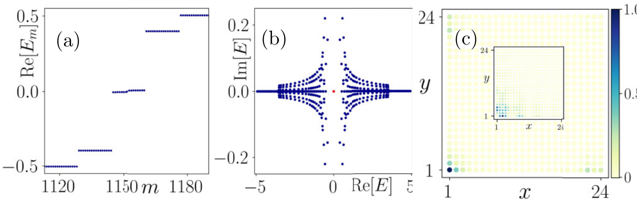

FIG. 4. (a) The real part of the energy spectrum, Re[E_m], obtained under OBC is shown as a function of the state index m. (b) The eigenvalue spectrum in the Re[E]-Im[E] plane is demonstrated. The corner state eigenvalues are indicated by the red dot. (c) The LDOS associated with the Re[E] $= 0$ is depicted in the 2D lattice. Inset: The LDOS associated with a bulk state with $E = -3.291\,226$. We choose $m_0 = -1.0$, while the other model parameters remain the same as mentioned in Fig. 3.

cases. The absolute value of energy is expected to vanish, i.e., $|E| = 0$ under OBC for $-2 - \gamma_2^2 < m_0 < 4 + 5\gamma_2^2$. However, numerical results suffer from finite-size effects as far as the exceptional boundaries are concerned [see the red lines in Fig. 3(f)]. The finite value of γ (NH effect) thus extends the Hermitian topological phase beyond its boundaries, leading to exceptional topological phases.

Moreover, we also analyze the eigenvalue spectrum, choosing a fixed value of m_0. As discussed before, we obtain four corner states when $3\gamma_2^2 < m_0 < 4 + 5\gamma_2^2$. The corresponding eigenvalue spectrum and LDOS, when the system exhibits four corner states, remain qualitatively the same, as depicted in Fig. 2 for the first-NN case. Thus, we do not repeat that analysis here. Rather, we choose the value of m_0 in such a way that we obtain 16 corner states. For this case, we show the real part of the eigenvalue spectrum, Re[E_m], close to Re[E] $= 0$ as a function of the state index m in Fig. 4(a), for a system obeying OBC. One can note the existence of 16 states at Re[E] $= 0$, which corresponds to localized corner modes. The finite separation from the exact Re[E] $= 0$ can be attributed to the finite-size effect. Nevertheless, in Fig. 4(b), we illustrate the eigenvalue spectrum in the Re[E]-Im[E] plane where the CS manifests itself in the symmetric profile of real energy. The corner modes are marked by the red dot. The line gap feature behaves in a similar way to the previous case. The corner modes have both real and imaginary parts of the eigenvalue equal to zero. We also illustrate the site-resolved LDOS distribution in Fig. 4(c). We find that the corner modes are mostly localized at only one corner of the 2D system, similar to the first-NN hopping case. Furthermore, we also observe the signature of the higher-order skin effect of the bulk states. To highlight this, we depict the LDOS associated with a bulk state in the inset of Fig. 4(c). It is evident that the bulk state is localized at the corners of the system.

C. Quadrupole winding number

We now investigate the topological invariant, namely, quadrupole winding number (QWN), by exploiting the CS. In the following discussion, we first illustrate the Hermitian version of QWN. Given the fact that CS constraints $CH_0(\mathbf{k})C^{-1} = -H_0(\mathbf{k})$, we can antidiagonalize the Hamiltonian in the basis of the CS operator spanned by U_C as follows [49,92]:

$$\tilde{H}_0 = U_C^\dagger H_0 U_C = \begin{pmatrix} 0 & h \\ \tilde{h} & 0 \end{pmatrix}. \tag{2}$$

Here, $\tilde{h} = h^\dagger$ if $\tilde{H}_0$ is Hermitian. We find $U_C C U_C^\dagger = \pm 1$, suggesting that CS can be classified into two kinds of sublattices, namely, A and B for $+$ and $-$ expectation values, respectively. This further entails that $U_C = U_C^A - U_C^B$, where $U_C^A = \sum_{\alpha \in A} |\alpha\rangle\langle\alpha|$ and $U_C^B = \sum_{\beta \in B} |\beta\rangle\langle\beta|$.

Employing singular-value decomposition of h, we obtain $h = U_A \Sigma U_B^\dagger$, where $U_{A,B}$ are unitary matrices and Σ denotes a diagonal matrix. Note that the diagonal elements of Σ are referred to as singular values. One can compute the flattened Hamiltonian Q, having eigenvalue ± 1, as follows [53]:

$$Q = \begin{pmatrix} 0 & q \\ q^\dagger & 0 \end{pmatrix}, \tag{3}$$

with $q = U_A U_B^\dagger$ being a unitary matrix. It has been shown that the winding number, derived using q and $q^\dagger$, is related to the relative polarization of the A and B sublattices. In a similar spirit, the winding number in the real space is given by [93]

$$\nu = \frac{1}{2\pi i} \mathrm{Tr}[\ln(\mathcal{X}_A \mathcal{X}_B^\dagger)], \tag{4}$$

where $\mathcal{X}_\sigma = U_\sigma^\dagger U_C^\sigma \mathcal{X} U_C^\sigma U_\sigma$ ($\sigma = A, B$) are unitary matrices. The operator $\mathcal{X}_\sigma$ denotes the sublattice dipole operator, which is the projection of the position operator onto the σ sector of the chiral basis. The position operator, i.e., the dipole operator $\mathcal{X} = \exp(2i\pi x/L)$, is defined on a periodic array of one-dimensional length L.

Now we turn to the two-dimensional system where the dipole operator $\mathcal{X}$ can be replaced by the quadrupole operator $\mathcal{Q} = \exp(2i\pi xy/L_x L_y)$. This results in the sublattice quadrupole operator $\mathcal{Q}_\sigma = U_\sigma^\dagger U_C^\sigma \mathcal{Q} U_C^\sigma U_\sigma$. Therefore, the QWN can be defined as [53]

$$N_{xy} = \frac{1}{2\pi i} \mathrm{Tr}[\ln(\mathcal{Q}_A \mathcal{Q}_B^\dagger)]. \tag{5}$$

This invariant is quantized to an integer number and predicts the number of topologically protected corner states at each corner of the 2D lattice.

We now examine the present situation with $\gamma \neq 0$, where the NH analog of QWN is discussed. Importantly, CS is also preserved for the NH Hamiltonian $C H_\gamma(\mathbf{k}) C^{-1} = -H_\gamma(\mathbf{k})$ allowing for the antidiagonal form of $\tilde{H}_\gamma$. At the same time, the definition of $U_C^{A,B}$ remains unaltered for the NH case. We adopt the bi-orthogonalized definitions of U_A and $U_B^\dagger$, obtained from the singular-value decomposition of h, to define $U_A^\dagger$ and U_B, respectively. One has to ensure $\sum_n |U_{\sigma,n}^R\rangle\langle U_{\sigma,n}^L| = \mathbb{1}$ and $\langle U_{\sigma,n}^L | U_{\sigma,m}^R\rangle = \delta_{mn}$, where $\sigma = A, B$ and $L(R)$ denotes the left (right) singular vectors. This results in left (right) singular vectors corresponding to right singular vectors $(U_B^\dagger)^\dagger \equiv U_B^R$ (left singular vectors $U_A^\dagger \equiv U_A^L$) as $U_B^\dagger \equiv U_B^L$ ($U_A \equiv U_A^R$). Therefore, sublattice quadrupole operator $\mathcal{Q}_\sigma$ takes the form $\mathcal{Q}_\sigma = U_\sigma^L U_C^\sigma \mathcal{Q} U_C^\sigma U_\sigma^R$. In addition, the non-Bloch form of momentum has to be incorporated while computing $\mathcal{Q}_\sigma$.

To be precise, the complex momentum $k_i \to k_i' - i\gamma_2$, with $i = x, y$, leads to the exponentially enhanced and suppressed hopping elements by the multiplicative factors $\exp(\gamma_1)$ and $\exp(-\gamma_1)$ [$\exp(\gamma_2)$ and $\exp(-\gamma_2)$] for first- [second-] NN models. We use the real-space form of the tight-binding model with the renormalized hopping amplitudes as follows: $\lambda_{1,2}^{s,h,f} \to \lambda_{1,2}^{s,h,f} \exp(\gamma_{1,2})$ and $\lambda_{1,2}^{s,h,f} \to \lambda_{1,2}^{s,h,f} \exp(-\gamma_{1,2})$, for forward and backward hopping amplitudes, respectively. We consider the real-space version of NH Hamiltonian H_γ with the above-mentioned renormalized hoppings in order to compute QWN. Altogether, this enables us to define the NH analog of QWN N_{xy} with dressed hopping and bi-orthogonalized definition. Note that the real part of N_{xy} exhibits a quantized value for the present case with $\gamma \neq 0$, as demonstrated below.

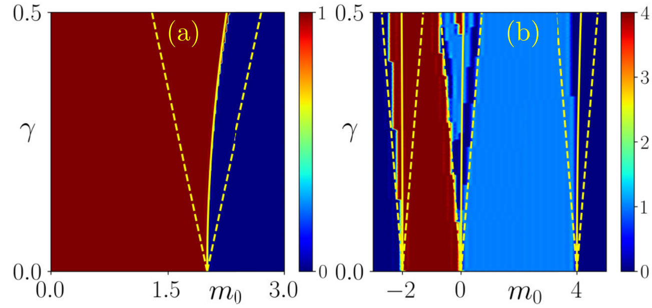

FIG. 5. The phase diagram in the m_0-γ plane for NH (a) first-NN and (b) second-NN hopping models. The color bar represents QWN N_{xy}. The phase boundary $m_0 = 2 + \gamma_1^2$ ($m_0 = 2 \pm \tilde{\gamma}$), obtained from OBC (PBC), between exceptional topological and trivial phases in (a) is identified by the yellow solid (dashed) line. The phase boundaries, associated with OBC (PBC), between topological phases hosting 16 and four corner modes and trivial phase, are given by $m_0 = 4 + 5\gamma_2^2$ ($m_0 = 4 \pm \tilde{\gamma}$), $m_0 = 3\gamma_2^2$ ($m_0 = \pm\tilde{\gamma}$), and $m_0 = -2 - \gamma_2^2$ ($m_0 = -2 \pm \tilde{\gamma}$), respectively, represented by the yellow solid (dashed) lines in (b).

We now discuss the phase diagram of the first- and second-NN NH model in the γ-m_0 plane in Figs. 5(a) and 5(b), respectively. Note that there exists four corner modes with $\mathrm{Re}[E] = 0$ for $m_0 < 2 + \gamma_1^2$, yielding $N_{xy} = 1$. This refers to the fact that there exists only one topological zero mode per corner [see Fig. 5(a)]. On the other hand, when $m_0 > 2 + \gamma_1^2$, the NH model does not host any topological phase and hence $N_{xy} = 0$. Hence, the topological phase boundary is $m_0 = 2 + \gamma_1^2$, which is indicated by the yellow solid line. This is also predicted from the complex energy spectrum with OBC. The yellow dashed lines in Fig. 5(a) represent $m_0 = 2 \pm \tilde{\gamma}$ lines, as predicted from the complex energy under PBC. Interestingly, the real-space invariant QWN fails to identify these phase boundaries. Unlike the Hermitian system, the phase boundaries between topological and trivial phases cannot be captured by the energy spectrum under OBC and PBC in the present NH case. This clearly suggests that the topological phase, predicted from the complex energy spectrum in OBC, is apprehended by the non-Bloch and bi-orthogonalized version of QWN. We note that the analytically derived phase boundaries are valid for $\gamma_{1,2} \ll 1$. Interestingly, the non-Hermiticity induces additional regions $-2 - \gamma_1^2 < m_0 < -2$ and $2 < m_0 < 2 + \gamma_1^2$ around $m_0 = \pm 2$ beyond the Hermitian phase boundaries. In Fig. 5(a), we only illustrate the positive m_0 window, where the NH SOTI phase is present for $m_0 < 2 + \gamma_1^2$.

We find qualitatively similar results in the case of the second-NN model, as shown in Fig. 5(b). In addition to the $N_{xy} = 1$ phase, we obtain the $N_{xy} = 4$ phase, where four zero-energy modes with $\text{Re}[E] = 0$ are present at each corner. While investigating the phase boundaries, it is expected to find $N_{xy} = 1$ (4) for $3\gamma_2^2 < m_0 < 4 + 5\gamma_2^2$ ($-2 - \gamma_2^2 < m_0 < 3\gamma_2^2$). For smaller strength of non-Hermiticity, i.e., $\gamma \to 0$, we find quantitative agreement between the analytical and numerical findings. The phase boundaries $m_0 = 4 + 5\gamma_2^2$, $3\gamma_2^2$, and $-2 - \gamma_2^2$, designated by the yellow solid line, do not fully comply with the N_{xy} profile for $\gamma > 0.1$. This can be due to more intricacies than just the finite-size effect. Interestingly, the following tendency is noticed: for $\tilde{\gamma} < m_0 < 4 + 5\gamma_2^2$, one obtains $N_{xy} = 1$, while within the regime $-2 - \tilde{\gamma} < m_0 < -\tilde{\gamma}$, N_{xy} acquires the value 4. Therefore, the non-Bloch and bi-orthogonalized version of QWN can quantitatively and qualitatively identify the phase boundaries of SOTI phases hosting four and 16 corner modes, starting from the trivial phases for $m_0 > 4 + 5\gamma_2^2$ and $m_0 < -2 - \tilde{\gamma}$, respectively, across which N_{xy} jumps between zero and finite values. The real-space invariant QWN is thus a useful topological marker to identify the exceptional phases for our NH system with OBC.

As mentioned earlier for the first-NN case, the Hermitian phase boundaries are modified due to the non-Hermiticity. For the second-NN Hermitian counterpart with $\gamma = 0$, one obtains SOTI phases $0 < m_0 < 4$ and $-2 < m_0 < 0$ hosting four and 16 zero-energy corner modes, respectively. The NH factor γ introduces four corner modes for positive values of m_0 beyond $m_0 = 4$ until $m_0 < 4 + 5\gamma_2^2$, as demonstrated in Fig. 5(b). The same applies to the negative values of m_0 where the 16 NH corner modes continue to exist for $|m_0| < 2 + \tilde{\gamma}$ beyond $m_0 = -2$. Importantly, in the second-NN SOTI model, the number of corner modes changes for positive and negative values of m_0, which is not the case for the first-NN SOTI model. Therefore, we would like to emphasize that the NH factor $\gamma \neq 0$ and the second-NN hoppings $\lambda_2^h, \lambda_2^s, \lambda_2^f \neq 0$ together modify the phase diagram in a complex manner such that the number of corner modes and their corresponding parameter window vary significantly as compared to the first-NN Hermitian model. It would be interesting to study in the future why the changes in QWN do not always follow the OBC energy gap closing lines. For example, $m_0 = -2 - \gamma_2^2$ and $m_0 = -2 - \tilde{\gamma}$ ($m_0 = 3\gamma_2^2$ and $m_0 = \pm\tilde{\gamma}$) phase boundaries around $m_0 = -2$ ($m_0 = 0$) can be investigated further for a better understanding of the interplay between the NH term and second-NN hoppings.

On the other hand, between the two SOTI phases with different number of corner modes (for $-\tilde{\gamma} < m_0 < \tilde{\gamma}$), we find $N_{xy} \neq 0$ as depicted in Fig. 5(b). In the complex energy analysis under OBC, we find macroscopic degeneracies with $\text{Re}[E] = 0$ for $-2 - \gamma_2^2 < m_0 < \tilde{\gamma}$. Likewise, the earlier first-NN case, N_{xy}, does not exhibit any jumps between finite and zero values around $m_0 = 4 \pm \tilde{\gamma}$ and $m_0 = -2 \pm \tilde{\gamma}$, which are predicted by the complex energy spectrum under PBC. On the contrary, $m_0 = \pm\tilde{\gamma}$ boundaries, predicted by the complex energy spectrum under PBC, are visible as N_{xy} changes between two finite values. The exceptional lines $m_0 = -2 \pm \tilde{\gamma}$, $\pm\tilde{\gamma}$, and $4 \pm \tilde{\gamma}$ obtained employing PBC are depicted by yellow dashed lines in Fig. 5(b). This agreement is surprising and yet to be explored in the future. However, there is an apparent discrepancy between the solid yellow lines and the numerically obtained N_{xy}. This mismatch is due to the fact that the mathematical form of non-Bloch transformation that we consider in the hopping terms while computing N_{xy}, employing PBC, is computed by employing a low-energy version of $H_\gamma(\mathbf{k})$. To obtain the low-energy spectrum of $H_\gamma(\mathbf{k})$, we expand the Hamiltonian around $\mathbf{k} = (0, 0)$. By doing that, we can obtain the phase boundary associated with the right part of Fig. 5(b). However, when we incorporate the second-NN hopping elements, the low-energy model around $\mathbf{k} = (0, 0)$ does not necessarily encapsulate all the phase transition lines. In that scenario, one should also consider a low-energy Hamiltonian around other momenta such as $\mathbf{k} = (\pm 2\pi/3, \pm 2\pi/3)$, depending upon the value of m_0. Nevertheless, this scenario adds substantial complexity to the problem as one should consider a different non-Bloch form for different m_0. Thus, finding a universal transformation to obtain the exact phase boundary in the NH second-NN hopping case still remains an interesting question and is beyond the scope of the present paper. Nevertheless, complex energy spectra under PBC might be useful for understanding the phase boundaries between two different topological phases.

IV. SUMMARY AND CONCLUSION

To summarize, in this article, we consider a second-NN hopping model in the presence of non-Hermiticity to investigate the emergence of second-order topological phases. By exploring the real part of the complex energy spectrum for the first- and second-NN NH models under OBC, we find that the former model only hosts four zero-energy corner modes, while the latter model can host four as well as 16 zero-energy corner modes as the hallmark of the NH SOTI phases. We compute the real-space invariant, namely, bi-orthogonalized QWN, by keeping in mind the non-Bloch form of the momentum to uniquely characterize the different topological phases. The phase boundaries captured by the above invariant can successfully mimic the emergence of NH SOTI phases out

TABLE I. Spatial symmetries and their operations.

Symmetry	Operation	Remarks
Mirror x	$M_x = \sigma_0 s_y$: $M_x H_\gamma(k_x, k_y) M_x^{-1} = H_\gamma(-k_x, k_y)$	Broken, when $\lambda_{1,2}^f, \gamma_x \neq 0$
Mirror y	$M_y = \sigma_z s_x$: $M_y H_\gamma(k_x, k_y) M_y^{-1} = H_\gamma(k_x, -k_y)$	Broken, when $\lambda_{1,2}^f, \gamma_y \neq 0$
Fourfold rotation	$C_4 = e^{-\frac{i\pi}{4}\sigma_z s_z}$: $C_4 H_\gamma(k_x, k_y) C_4^{-1} = H_\gamma(-k_y, k_x)$	Broken, when $\lambda_{1,2}^f, \gamma_{x,y} \neq 0$
Mirror rotation I	$M_{xy} = C_4 M_y$: $M_{xy} H_\gamma(k_x, k_y) M_{xy}^{-1} = H_\gamma(k_y, k_x)$	Broken, when $\gamma_x \neq \gamma_y$
Mirror rotation II	$M_{x\bar{y}} = C_4 M_x$: $M_{x\bar{y}} H_\gamma(k_x, k_y) M_{x\bar{y}}^{-1} = H_\gamma(-k_y, -k_x)$	Broken, when $\gamma_x \neq \gamma_y$

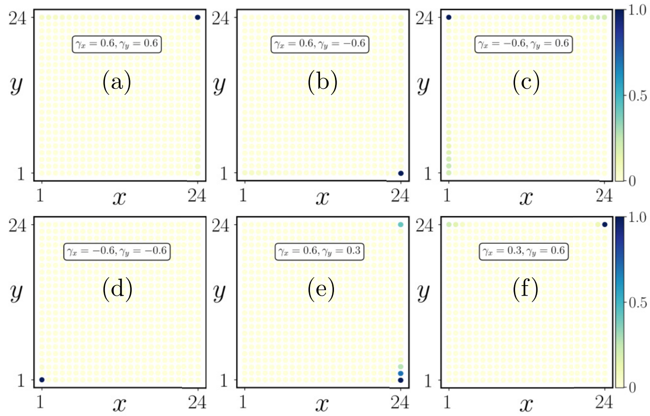

FIG. 6. In the 2D domain, we illustrate the LDOS spectrum associated with the $E = 0$ states choosing different values of γ_x and γ_y: (a) $\gamma_x = \gamma_y = 0.6$, (b) $\gamma_x = -\gamma_y = 0.6$, (c) $\gamma_x = -\gamma_y = -0.6$, (d) $\gamma_x = \gamma_y = -0.6$, (e) $\gamma_x = 0.6$, $\gamma_y = 0.3$, and (f) $\gamma_x = 0.3$, $\gamma_y = 0.6$. We choose $m_0 = 1.0$, while the other model parameters remain the same as mentioned in Fig. 1.

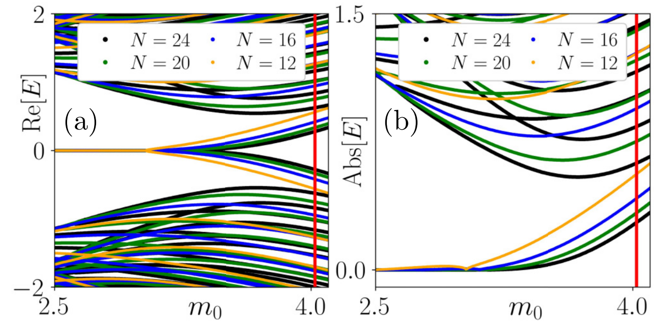

FIG. 7. In (a) and (b), we demonstrate Re$[E]$ and Abs$[E]$ close to the rightmost phase transition line in Figs. 3(d) and 3(f), choosing different system sizes, respectively.

of the trivial phases, as demonstrated by the complex energy dispersion under OBC for both the first- and second-NN models. The topological phase boundary between two different topological phases, observed in the second-NN model, can be anticipated from the complex energy spectrum under PBC for the above model. In the future, one can include disorder to study the exceptional topological Anderson insulators hosting corner modes where a generalized version of the presently adopted real-space topological index will have to be examined.

ACKNOWLEDGMENTS

A.K.G. and A.S. acknowledge SAMKHYA: High-Performance Computing Facility provided by Institute of Physics, Bhubaneswar, for numerical computations. T.N. acknowledges the NFSG “NFSG/HYD/2023/H0911” from BITS Pilani.

APPENDIX A: SPATIAL SYMMETRIES AND LOCALIZATION OF CORNER STATES FOR ASYMMETRIC γ

In Table I, we list all the symmetries that the model Hamiltonian $H_\gamma(\mathbf{k})$ breaks or preserves. As discussed in the main text, the mirror rotation symmetry M_{xy} plays a crucial role in the localization of the corner states. In Fig. 6, we demonstrate the LDOS associated with the $E = 0$ states choosing different values of γ_x and γ_y. Note that in the main text, we always consider $\gamma_x = \gamma_y = \gamma$. In Figs. 6(a)–6(d), we illustrate the case when γ_x and γ_y carry the same amplitude, but can have different signs for a NH first-NN Hamiltonian model. We observe that depending upon the signs of γ_x and γ_y, the corner modes occupy different corners of the system. In contrast, when $\gamma_x \neq \gamma_y$, i.e., the mirror rotation symmetries are broken, the corner states can occupy more than one corner [see Figs. 6(e) and 6(f)]. However, it is to be noted that the localization at different corners carries different weights.

APPENDIX B: FINITE-SIZE SCALING WITH SECOND-NN NH HOPPING MODEL

As discussed in the main text, the rightmost part of the phase boundary [in Figs. 3(d) and 3(f)] corresponding to the second-NN NH Hamiltonian encounters finite-size scaling. Here, we explicitly exhibit variation of the eigenvalue spectra considering different system sizes. In particular, we demonstrate the real (Re$[E]$) and absolute (Abs$[E]$) parts of the eigenvalue spectra close to the rightmost phase transition line of Figs. 3(d) and 3(f), choosing different system sizes ($N = 12, 16, 20, 24$) in Fig. 7. One can evidently observe from Figs. 7(a) and 7(b) that as we increase the system size, the zero-energy states in the eigenvalue spectra move towards the analytically obtained phase transition line (red). However, the translation towards the phase transition line as a function of the system size appears to be slower in nature.

[1] M. Z. Hasan and C. L. Kane, Colloquium: Topological insulators, Rev. Mod. Phys. **82**, 3045 (2010).

[2] M. Sato and Y. Ando, Topological superconductors: A review, Rep. Prog. Phys. **80**, 076501 (2017).

[3] F. D. M. Haldane, Model for a quantum Hall effect without Landau levels: Condensed-matter realization of the“parity anomaly”, Phys. Rev. Lett. **61**, 2015 (1988).

[4] C. L. Kane and E. J. Mele, Z_2 topological order and the quantum spin Hall effect, Phys. Rev. Lett. **95**, 146802 (2005).

[5] B. A. Bernevig, T. L. Hughes, and S.-C. Zhang, Quantum spin Hall effect and topological phase transition in HgTe quantum wells, Science **314**, 1757 (2006).

[6] W. A. Benalcazar, B. A. Bernevig, and T. L. Hughes, Quantized electric multipole insulators, Science **357**, 61 (2017).

[7] W. A. Benalcazar, B. A. Bernevig, and T. L. Hughes, Electric multipole moments, topological multipole moment pumping, and chiral hinge states in crystalline insulators, Phys. Rev. B **96**, 245115 (2017).

[8] Z. Song, Z. Fang, and C. Fang, $(d-2)$-dimensional edge states of rotation symmetry protected topological states, Phys. Rev. Lett. **119**, 246402 (2017).
[9] J. Langbehn, Y. Peng, L. Trifunovic, F. von Oppen, and P. W. Brouwer, Reflection-symmetric second-order topological insulators and superconductors, Phys. Rev. Lett. **119**, 246401 (2017).
[10] F. Schindler, A. M. Cook, M. G. Vergniory, Z. Wang, S. S. Parkin, B. A. Bernevig, and T. Neupert, Higher-order topological insulators, Sci. Adv. **4**, eaat0346 (2018).
[11] S. Franca, J. van den Brink, and I. C. Fulga, An anomalous higher-order topological insulator, Phys. Rev. B **98**, 201114 (2018).
[12] Z. Wang, B. J. Wieder, J. Li, B. Yan, and B. A. Bernevig, Higher-order topology, monopole nodal lines, and the origin of large Fermi arcs in transition metal dichalcogenides $X\mathrm{Te}_2$ ($X=$ Mo, W), Phys. Rev. Lett. **123**, 186401 (2019).
[13] D. Călugăru, V. Juričić, and B. Roy, Higher-order topological phases: A general principle of construction, Phys. Rev. B **99**, 041301 (2019).
[14] P. Szumniak, D. Loss, and J. Klinovaja, Hinge modes and surface states in second-order topological three-dimensional quantum Hall systems induced by charge density modulation, Phys. Rev. B **102**, 125126 (2020).
[15] X. Ni, M. Li, M. Weiner, A. Alù, and A. B. Khanikaev, Demonstration of a quantized acoustic octupole topological insulator, Nat. Commun. **11**, 2108 (2020).
[16] B. Xie, H. Wang, X. Zhang, P. Zhan, J. Jiang, M. Lu, and Y. Chen, Higher-order band topology, Nat. Rev. Phys. **3**, 520 (2021).
[17] S. Saha, T. Nag, and S. Mandal, Multiple higher-order topological phases with even and odd pairs of zero-energy corner modes in a C3symmetry broken model, Europhys. Lett. **142**, 56002 (2023).
[18] X. Zhu, Tunable Majorana corner states in a two-dimensional second-order topological superconductor induced by magnetic fields, Phys. Rev. B **97**, 205134 (2018).
[19] T. Liu, J. J. He, and F. Nori, Majorana corner states in a two-dimensional magnetic topological insulator on a high-temperature superconductor, Phys. Rev. B **98**, 245413 (2018).
[20] Z. Yan, F. Song, and Z. Wang, Majorana corner modes in a high-temperature platform, Phys. Rev. Lett. **121**, 096803 (2018).
[21] Y. Wang, M. Lin, and T. L. Hughes, Weak-pairing higher order topological superconductors, Phys. Rev. B **98**, 165144 (2018).
[22] R.-X. Zhang, W. S. Cole, and S. Das Sarma, Helical hinge Majorana modes in iron-based superconductors, Phys. Rev. Lett. **122**, 187001 (2019).
[23] R.-X. Zhang, W. S. Cole, X. Wu, and S. Das Sarma, Higher-order topology and nodal topological superconductivity in Fe(Se,Te) heterostructures, Phys. Rev. Lett. **123**, 167001 (2019).
[24] Y. Volpez, D. Loss, and J. Klinovaja, Second-order topological superconductivity in π-junction Rashba layers, Phys. Rev. Lett. **122**, 126402 (2019).
[25] Z. Yan, Majorana corner and hinge modes in second-order topological insulator/superconductor heterostructures, Phys. Rev. B **100**, 205406 (2019).
[26] S. A. A. Ghorashi, X. Hu, T. L. Hughes, and E. Rossi, Second-order Dirac superconductors and magnetic field induced Majorana hinge modes, Phys. Rev. B **100**, 020509 (2019).
[27] Y.-J. Wu, J. Hou, Y.-M. Li, X.-W. Luo, X. Shi, and C. Zhang, In-plane Zeeman-field-induced Majorana corner and hinge modes in an s-wave superconductor heterostructure, Phys. Rev. Lett. **124**, 227001 (2020).
[28] K. Laubscher, D. Chughtai, D. Loss, and J. Klinovaja, Kramers pairs of Majorana corner states in a topological insulator bilayer, Phys. Rev. B **102**, 195401 (2020).
[29] B. Roy, Higher-order topological superconductors in $\mathcal{P}$-, $\mathcal{T}$-odd quadrupolar Dirac materials, Phys. Rev. B **101**, 220506 (2020).
[30] S.-B. Zhang, W. B. Rui, A. Calzona, S.-J. Choi, A. P. Schnyder, and B. Trauzettel, Topological and holonomic quantum computation based on second-order topological superconductors, Phys. Rev. Res. **2**, 043025 (2020).
[31] M. Kheirkhah, Z. Yan, and F. Marsiglio, Vortex-line topology in iron-based superconductors with and without second-order topology, Phys. Rev. B **103**, L140502 (2021).
[32] Z. Yan, Higher-order topological odd-parity superconductors, Phys. Rev. Lett. **123**, 177001 (2019).
[33] J. Ahn and B.-J. Yang, Higher-order topological superconductivity of spin-polarized fermions, Phys. Rev. Res. **2**, 012060 (2020).
[34] X.-J. Luo, X.-H. Pan, and X. Liu, Higher-order topological superconductors based on weak topological insulators, Phys. Rev. B **104**, 104510 (2021).
[35] Q. Wang, C.-C. Liu, Y.-M. Lu, and F. Zhang, High-temperature Majorana corner states, Phys. Rev. Lett. **121**, 186801 (2018).
[36] A. K. Ghosh, T. Nag, and A. Saha, Hierarchy of higher-order topological superconductors in three dimensions, Phys. Rev. B **104**, 134508 (2021).
[37] B. Roy and V. Juričić, Mixed-parity octupolar pairing and corner Majorana modes in three dimensions, Phys. Rev. B **104**, L180503 (2021).
[38] T. Li, M. Geier, J. Ingham, and H. D. Scammell, Higher-order topological superconductivity from repulsive interactions in kagome and honeycomb systems, 2D Mater. **9**, 015031 (2022).
[39] A. K. Ghosh, T. Nag, and A. Saha, Systematic generation of the cascade of anomalous dynamical first- and higher-order modes in Floquet topological insulators, Phys. Rev. B **105**, 115418 (2022).
[40] A. K. Ghosh, T. Nag, and A. Saha, Dynamical construction of quadrupolar and octupolar topological superconductors, Phys. Rev. B **105**, 155406 (2022).
[41] W. DeGottardi, M. Thakurathi, S. Vishveshwara, and D. Sen, Majorana fermions in superconducting wires: Effects of long-range hopping, broken time-reversal symmetry, and potential landscapes, Phys. Rev. B **88**, 165111 (2013).
[42] Y. Niu, S. B. Chung, C.-H. Hsu, I. Mandal, S. Raghu, and S. Chakravarty, Majorana zero modes in a quantum Ising chain with longer-ranged interactions, Phys. Rev. B **85**, 035110 (2012).
[43] D. Xie, W. Gou, T. Xiao, B. Gadway, and B. Yan, Topological characterizations of an extended Su-Schrieffer-Heeger model, npj Quantum Inf. **5**, 55 (2019).
[44] R. G. Dias and A. M. Marques, Long-range hopping and indexing assumption in one-dimensional topological insulators, Phys. Rev. B **105**, 035102 (2022).

[45] D. Mondal and T. Nag, Persistent anomaly in dynamical quantum phase transition in long-range non-Hermitian p-wave Kitaev chian, Eur. Phys. J. B **97**, 59 (2024).
[46] M. Thakurathi, A. A. Patel, D. Sen, and A. Dutta, Floquet generation of Majorana end modes and topological invariants, Phys. Rev. B **88**, 155133 (2013).
[47] A. P. Schnyder, S. Ryu, A. Furusaki, and A. W. W. Ludwig, Classification of topological insulators and superconductors in three spatial dimensions, Phys. Rev. B **78**, 195125 (2008).
[48] A. Kitaev, Periodic table for topological insulators and superconductors, in *Advances in Theoretical Physics: Landau Memorial Conference*, AIP Conf Proc. No. 1134 (AIP, New York, 2009), p. 22.
[49] S. Ryu, A. P. Schnyder, A. Furusaki, and A. W. Ludwig, Topological insulators and superconductors: Tenfold way and dimensional hierarchy, New J. Phys. **12**, 065010 (2010).
[50] S. Ryu and Y. Hatsugai, Topological origin of zero-energy edge states in particle-hole symmetric systems, Phys. Rev. Lett. **89**, 077002 (2002).
[51] J. C. Y. Teo and C. L. Kane, Topological defects and gapless modes in insulators and superconductors, Phys. Rev. B **82**, 115120 (2010).
[52] M. Nakahara, *Geometry, Topology and Physics* (IOP Publishing, Bristol, Philadelphia, 2018).
[53] W. A. Benalcazar and A. Cerjan, Chiral-symmetric higher-order topological phases of matter, Phys. Rev. Lett. **128**, 127601 (2022).
[54] N. Parappurath, F. Alpeggiani, L. Kuipers, and E. Verhagen, Direct observation of topological edge states in silicon photonic crystals: Spin, dispersion, and chiral routing, Sci. Adv. **6**, eaaw4137 (2020).
[55] Y. Yang, Z. Gao, H. Xue, L. Zhang, M. He, Z. Yang, R. Singh, Y. Chong, B. Zhang, and H. Chen, Realization of a three-dimensional photonic topological insulator, Nature (London) **565**, 622 (2019).
[56] S. Malzard, C. Poli, and H. Schomerus, Topologically protected defect states in open photonic systems with non-Hermitian charge-conjugation and parity-time symmetry, Phys. Rev. Lett. **115**, 200402 (2015).
[57] A. Regensburger, C. Bersch, M.-A. Miri, G. Onishchukov, D. N. Christodoulides, and U. Peschel, Parity–time synthetic photonic lattices, Nature (London) **488**, 167 (2012).
[58] R. El-Ganainy, K. G. Makris, M. Khajavikhan, Z. H. Musslimani, S. Rotter, and D. N. Christodoulides, Non-Hermitian physics and PT symmetry, Nat. Phys. **14**, 11 (2018).
[59] M. M. Denner, A. Skurativska, F. Schindler, M. H. Fischer, R. Thomale, T. Bzdušek, and T. Neupert, Exceptional topological insulators, Nat. Commun. **12**, 5681 (2021).
[60] E. J. Bergholtz and J. C. Budich, Non-Hermitian Weyl physics in topological insulator ferromagnet junctions, Phys. Rev. Res. **1**, 012003 (2019).
[61] Y.-B. Yang, K. Li, L.-M. Duan, and Y. Xu, Higher-order topological Anderson insulators, Phys. Rev. B **103**, 085408 (2021).
[62] P. San-Jose, J. Cayao, E. Prada, and R. Aguado, Majorana bound states from exceptional points in non-topological superconductors, Sci. Rep. **6**, 21427 (2016).
[63] V. Kozii and L. Fu, Non-Hermitian topological theory of finite-lifetime quasiparticles: Prediction of bulk Fermi arc due to exceptional point, arXiv:1708.05841.
[64] T. Yoshida, R. Peters, and N. Kawakami, Non-Hermitian perspective of the band structure in heavy-fermion systems, Phys. Rev. B **98**, 035141 (2018).
[65] H. Shen and L. Fu, Quantum oscillation from in-gap states and a non-Hermitian Landau level problem, Phys. Rev. Lett. **121**, 026403 (2018).
[66] Z. H. Musslimani, K. G. Makris, R. El-Ganainy, and D. N. Christodoulides, Optical solitons in $\mathcal{PT}$ periodic potentials, Phys. Rev. Lett. **100**, 030402 (2008).
[67] K. G. Makris, R. El-Ganainy, D. N. Christodoulides, and Z. H. Musslimani, Beam dynamics in $\mathcal{PT}$ symmetric optical lattices, Phys. Rev. Lett. **100**, 103904 (2008).
[68] S. Yao, F. Song, and Z. Wang, Non-Hermitian Chern bands, Phys. Rev. Lett. **121**, 136802 (2018).
[69] K. Kawabata, K. Shiozaki, M. Ueda, and M. Sato, Symmetry and topology in non-Hermitian physics, Phys. Rev. X **9**, 041015 (2019).
[70] E. J. Bergholtz, J. C. Budich, and F. K. Kunst, Exceptional topology of non-Hermitian systems, Rev. Mod. Phys. **93**, 015005 (2021).
[71] K. Sone, Y. Ashida, and T. Sagawa, Exceptional non-Hermitian topological edge mode and its application to active matter, Nat. Commun. **11**, 5745 (2020).
[72] A. K. Ghosh and A. M. Black-Schaffer, Majorana zero-modes in a dissipative Rashba nanowire, SciPost Phys. **17**, 036 (2024).
[73] S. Yao and Z. Wang, Edge states and topological invariants of non-Hermitian systems, Phys. Rev. Lett. **121**, 086803 (2018).
[74] F. K. Kunst, E. Edvardsson, J. C. Budich, and E. J. Bergholtz, Biorthogonal bulk-boundary correspondence in non-Hermitian systems, Phys. Rev. Lett. **121**, 026808 (2018).
[75] T. Liu, Y.-R. Zhang, Q. Ai, Z. Gong, K. Kawabata, M. Ueda, and F. Nori, Second-order topological phases in non-Hermitian systems, Phys. Rev. Lett. **122**, 076801 (2019).
[76] T. Helbig, T. Hofmann, S. Imhof, M. Abdelghany, T. Kiessling, L. W. Molenkamp, C. H. Lee, A. Szameit, M. Greiter, and R. Thomale, Generalized bulk-boundary correspondence in non-Hermitian topolectrical circuits, Nat. Phys. **16**, 747 (2020).
[77] D. S. Borgnia, A. J. Kruchkov, and R.-J. Slager, Non-Hermitian boundary modes and topology, Phys. Rev. Lett. **124**, 056802 (2020).
[78] R. Koch and J. C. Budich, Bulk-boundary correspondence in non-Hermitian systems: Stability analysis for generalized boundary conditions, Europhys. J. D **74**, 70 (2020).
[79] H.-G. Zirnstein, G. Refael, and B. Rosenow, Bulk-boundary correspondence for non-Hermitian Hamiltonians via Green functions, Phys. Rev. Lett. **126**, 216407 (2021).
[80] Y. Takane, Bulk-boundary correspondence in a non-Hermitian Chern insulator, J. Phys. Soc. Jpn. **90**, 033704 (2021).
[81] K. Kawabata, M. Sato, and K. Shiozaki, Higher-order non-Hermitian skin effect, Phys. Rev. B **102**, 205118 (2020).
[82] C. M. Bender, Making sense of non-Hermitian Hamiltonians, Rep. Prog. Phys. **70**, 947 (2007).
[83] W. D. Heiss, The physics of exceptional points, J. Phys. A: Math. Theor. **45**, 444016 (2012).
[84] B. Pérez-González, M. Bello, A. Gómez-León, and G. Platero, Interplay between long-range hopping and disorder in topological systems, Phys. Rev. B **99**, 035146 (2019).
[85] F. A. An, E. J. Meier, and B. Gadway, Engineering a flux-dependent mobility edge in disordered zigzag chains, Phys. Rev. X **8**, 031045 (2018).

[86] H.-C. Hsu and T.-W. Chen, Topological Anderson insulating phases in the long-range Su-Schrieffer-Heeger model, Phys. Rev. B **102**, 205425 (2020).
[87] A. K. Ghosh and T. Nag, Non-Hermitian higher-order topological superconductors in two dimensions: Statics and dynamics, Phys. Rev. B **106**, L140303 (2022).
[88] H. Liu, J.-K. Zhou, B.-L. Wu, Z.-Q. Zhang, and H. Jiang, Real-space topological invariant and higher-order topological Anderson insulator in two-dimensional non-Hermitian systems, Phys. Rev. B **103**, 224203 (2021).
[89] H. Liu, M. Lu, Z.-Q. Zhang, and H. Jiang, Modified generalized Brillouin zone theory with on-site disorder, Phys. Rev. B **107**, 144204 (2023).
[90] C. Rangi, K.-M. Tam, and J. Moreno, Engineering a non-Hermitian second-order topological insulator state in quasicrystals, Phys. Rev. B **109**, 064203 (2024).
[91] X. Ji, W. Ding, Y. Chen, and X. Yang, Non-Hermitian second-order topological superconductors, Phys. Rev. B **109**, 125420 (2024).
[92] C.-K. Chiu, J. C. Y. Teo, A. P. Schnyder, and S. Ryu, Classification of topological quantum matter with symmetries, Rev. Mod. Phys. **88**, 035005 (2016).
[93] L. Lin, Y. Ke, and C. Lee, Real-space representation of the winding number for a one-dimensional chiral-symmetric topological insulator, Phys. Rev. B **103**, 224208 (2021).